Acta Materialia 206 (2021) 116638

Contents lists available at ScienceDirect

Acta Materialia

journal homepage: www.elsevier.com/locate/actamat

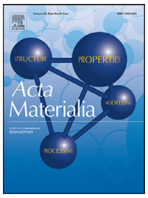

# Chemical-Affinity Disparity and Exclusivity Drive Atomic Segregation, Short-Range Ordering, and Cluster Formation in High-Entropy Alloys

Shuai Chen[1], Zachary H. Aitken[1], Subrahmanyam Pattamatta[2], Zhaoxuan Wu[2], Zhi Gen Yu[1], Rajarshi Banerjee[3], David J. Srolovitz[2,*], Peter K. Liaw[4,*], Yong-Wei Zhang[1,*]

[1] *Institute of High Performance Computing, A*STAR, 138632 Singapore*
[2] *Department of Materials Science and Engineering, City University of Hong Kong, Tat Chee Avenue, Kowloon, Hong Kong, China*
[3] *Department of Materials Science and Engineering, University of North Texas, Denton, TX, 76207, USA*
[4] *Department of Materials Science and Engineering, The University of Tennessee, Knoxville, TN 37996, USA*

A R T I C L E I N F O

*Article history:*
Received 15 August 2020
Revised 8 January 2021
Accepted 9 January 2021
Available online 17 January 2021

A B S T R A C T

Recently, atomic segregation, short-range ordering, and cluster formation have been observed experimentally in high-entropy alloys (HEAs). Differences in the atomic size and electronegativity of constituent elements were proposed to be the underlying cause of such ordering. Here, we investigated two HEAs, CoCuFeNiPd and CoCuFeNiTi, using a combination of Monte Carlo and molecular dynamic simulations. Our results show that the CoCuFeNiPd HEA exhibits much stronger atomic segregation and short-range ordering than the CoCuFeNiTi HEA, despite the larger differences in the relative atomic size and electronegativity of Ti with other constituent elements, as compared to those of Pd, suggesting that the differences in the atomic size and electronegativity alone are insufficient to explain the simulation results. We find that it is the chemical-affinity disparity and exclusivity between Ti (Pd) with the remaining species that lead to the different clustering behavior in these two HEAs. Specifically, three conditions for strong atomic segregation and short-range ordering are identified: 1. a large chemical-affinity disparity amongst the chemical elements; 2. a high chemical-element exclusivity in low-, medium-, and high-energy clusters; and 3. a net energy reduction associated with low- and medium-energy-cluster formation that compensates for the energy increase associated with high-energy-cluster formation. Our findings are in agreement with experimental results reported in literature, and highlight the importance of chemical-affinity disparity and exclusivity in influencing the microstructure of HEAs, explain the origin of high-energy-cluster formation in HEAs, and provide guidelines for designing HEAs with excellent properties.

## 1. Introduction

Conventional design of metallic alloys is based on the concept of adding small amounts of alloying elements to one or two principal elements. Aluminum alloys [1], magnesium alloys [2], and titanium alloys [3] are common examples. In 2004, Yeh et al. [4] and Cantor et al. [5] proposed a novel category of multi-principal component alloys consisting of five or more metallic elements at atomic concentrations typically ranging between 5 and 35 atomic percent (at. %), and widely referred to as "high-entropy alloys" (HEAs). Since then, HEAs have attracted increasing attention due to their excellent mechanical properties, such as outstanding structural stability [6] and a fascinating balance between strength and ductility [7,8], which are important for structural applications. Multiple studies have shown that mechanical properties of HEAs are sensitive to both changes in chemical compositions and processing conditions [9-11]. Controlling processing pathways [12,13] provides new opportunities to tune HEA microstructures to achieve desired mechanical properties for specific engineering applications. An in-depth understanding of HEA microstructure formation is a prerequisite to a rational HEA design [14,15].

Recently, Ding et al. [16] synthesized the face-centered-cubic (FCC) HEAs, CoCrFeNiPd and CoCrFeNiMn. The former exhibited a higher yield strength than the latter, with similar strain hardening and tensile ductility. They suggested that the important differences between these two HEAs were associated with the fact that Pd has a much different atomic size and electronegativity relative to the other four elements (Co, Cr, Fe, and Ni) than does Mn. As a result, there was a greater tendency for the formation of atomic clusters and short-range ordering (SRO) [17,18] in CoCrFeNiPd

---

* Corresponding authors:
*E-mail addresses:* srol@cityu.edu.sg (D.J. Srolovitz), pliaw@utk.edu (P.K. Liaw), zhangyw@ihpc.a-star.edu.sg (Y.-W. Zhang).

https://doi.org/10.1016/j.actamat.2021.116638

than CoCrFeNiMn. Therefore, deformation that tends to disrupt SRO should be more difficult (occur at a higher stress level) in CoCrFeNiPd than in CoCrFeNiMn. In order to understand the role of SRO on the deformation of and dislocations in HEAs, hybrid molecular dynamics (MD) and Monte Carlo (MC) simulations were performed on random and annealed $Co_{30}Fe_{16.67}Ni_{36.67}Ti_{16.67}$ alloys [19]. Their key observation was that the interplay between the misfit interaction and SRO affects the overall critical resolved shear stress and concluded that overall strength results from a competition between these two factors.

Zhang et al. [17] measured the SRO in a CoCrNi medium-entropy alloy (MEA) using energy-filtered transmission electron microscopy. They found that increases in SRO resulted in higher stacking-fault energies and hardness. Jian et al. [20] applied hybrid MD and MC methods to simulate the nucleation and evolution of dislocations and nanotwins with strain in a CoCrNi MEA. Their results suggest that the strain required to nucleate Shockley partial dislocations increases with SRO and that this is an important determinant of yield strength. In the same alloy system, Li et al. [21] reported that increasing SRO enhances the ruggedness of the energy landscape and the activation barriers governing dislocation activity, thereby boosting the strength. Yin et al. [22] examined the yield strength and misfit volume in the same MEA system to determine whether SRO has a measurable effect on mechanical properties. They concluded that under typical processing conditions (e.g., annealing at $>600°$C), the SRO was negligible/had no systematic effect on strength of this MEA. As the number of the components increases, the formation of SRO becomes more complicated in HEAs due to their complex local atomic environment, as compared with that in binary alloys or MEAs [23].

Recent work has shown that ductile $L1_2$ phase ($Ni_3Al$-type) clusters/coherent precipitates can be formed within a high-strength FCC matrix [24]. Arguments, such as SRO and cluster formation, are common in the MEA/HEA community and revolve around the issue of what the relative chemical affinities of the different constituent elements for each other are. Hence, the following critical questions naturally arise. Are the differences in the atomic size and electronegativity the only driving forces responsible for the SRO in HEAs? Can the differences in chemical affinities amongst the constituents drive atomic segregation, SRO, and cluster formation? Clearly, answers to these critical questions are of great importance to guide the design and processing of HEAs to achieve high-performance mechanical properties.

Since atomic segregation, SRO, and cluster formation are all atomic-level phenomena, it is difficult to directly observe the formation and evolution of atomic clustering in experiments. Therefore, a powerful tool to gain a deep understanding of the underlying origin of the formation of atomic clustering in HEAs at the atomic scale is essential. Atomistic-simulation techniques, especially MD [25-27] and MC simulations [28-30], as well as density functional theory (DFT) calculations [31-33], can provide insight into atomic-scale phenomena of HEAs, which complement experiments and help clarify the underlying mechanisms behind some of these experimental observations. For example, Fu et al. [34] experimentally-synthesized a single-phase (FCC) nanocrystalline $CoNiFeAl_{0.3}Cu_{0.7}$ HEA by mechanical alloying, followed by consolidation and spark plasma sintering. This HEA showed a compressive yield strength of 1.8 GPa, which was dramatically higher than that of previously-reported FCC HEAs (0.2 GPa to 0.6 GPa) [35-38]. Li et al. [27] performed MD simulations with the same chemical compositions and similar grain sizes as in the experiments of Fu et al. [34] from which they concluded that the high strength and ductility of the nanocrystalline $CoNiFeAl_{0.3}Cu_{0.7}$ HEA were associated with a strain-induced phase transformation from FCC to body-centered-cubic (BCC) structures. Based on transmission electron microscopy and MD simulations, Choudhuri et al. [39] suggested that $B_2$ grains enhanced deformation twinning by raising local stress levels, consequently forming substantially thicker twins, as compared to the single-phase FCC $CoNiFeAl_{0.3}Cr$ HEAs. Sharma et al. [40] also found that the $Al_{0.1}CrCoFeNi$ HEA exhibited significant chemical clustering over a wide temperature range based on high-strain compression in MD simulations. MC is often a more convenient and efficient technique to obtain energetically-favourable atomic configurations in an HEA, as compared with MD due to time-scale limitations of MD. Combined MC and MD simulations provide a powerful route to explore the effects of differences in chemical affinities among the constituent elements on atomic segregation, SRO, and cluster formation. However, formation, characterization, and modelling of SRO in compositionally complex HEAs, as well as their effects on mechanical and physical behaviors are still far from being fully understood [23].

Here, we perform iterative MC and MD simulations to obtain energetically-favourable atomic configurations of CoCuFeNiPd and CoCuFeNiTi HEAs. MC is used to exchange atoms of different types, and MD is employed to relax the system via local atomic displacements. Because our simulations are performed, using empirical interatomic potentials, we validate our MC/MD results via a series of DFT calculations. Our analyses of the atomic structures generated in these systems are based on local compositions and Warren-Cowley parameters (WCPs), which are shown to be consistent with Ding et al.'s experimental observations [16]. Analyses of the atomic configuration and WCPs show that atomic segregation and SRO are less pronounced in the CoCuFeNiTi HEA than in the CoCuFeNiPd HEA. Since the relative atomic size and electronegativity differences of Ti (compared with the other HEA constituents: Co, Cu, Fe, and Ni) are larger than those for Pd, the approach proposed by Ding et al. [16] is unable to explain the weaker atomic segregation and SRO in the CoCuFeNiTi HEA. Our analyses show that the chemical-affinity disparity and exclusivity between Ti (Pd) with the other HEA constituents (Co, Cu, Fe, and Ni) are responsible for the differences in the atomic segregation, SRO, and the cluster formation in these two HEAs. The underlying reason for the strong atomic segregation of the CoCuFeNiPd HEA is because the chemical elements in the low-energy clusters (Ni-Ni, Co-Co, and Co-Ni), the medium-energy clusters (Fe-Pd, Fe-Fe, and Pd-Pd), and the high-energy cluster (Cu-Cu) do not intermix. Moreover, the energy reduction due to low- and medium-energy-cluster formation is able to compensate for the energy increase due to the high-energy-cluster formation, thereby reducing the overall system energy. On the other hand, Ti has a strong chemical affinity with most of the constituent atoms (Ti, Fe, Ni, and Co), and many of the elements are involved in the formation of atomic clusters across different energy levels, leading to the intermixing of atomic clusters and the weakening of segregation in the CoCuFeNiTi HEA. Our simulation results are consistent with a wide range of experimental observations [37,41], and highlight the importance of chemical-affinity disparity and exclusivity in determining and designing HEA microstructures.

## 2. Methods

### 2.1. MD and MC simulations

The large-scale atomic/molecular massively-parallel simulator (LAMMPS) package [42] was used to perform MD and MC simulations. The simulations employed embedded atom model (EAM) potential parameters of Zhou et al. [43,44]. Previous MD simulations of $CoNiFeAl_{0.3}Cu_{0.7}$ [27] using these potentials reproduced key aspects of the experimental compressive behavior of this alloy [34]. Li et al. [45] also recently applied this potential to study the compressive property of an $Al_{0.25}CoFeNiCu_{0.75}$ HEA to understand the effect of alloying on deformation twinning. We also employed this potential to investigate the phase stability and the mechanical response of $Al_xCoFeNiCu_{1-x}$ (x = 0.1 to 0.9) [46] and obtained reasonable results, compared with experimental measurements [47,34]. To understand the atomic-segregation effects observed in the experiments of Ding et al. [16], we applied the same EAM potential [43,44] to study FCC HEAs. The initial lattice constant of the FCC structure was 3.6 Å [16], and the simulation cell dimensions were $4.68 \times 4.68 \times 4.68$ $nm^3$ (i.e., 8,788 atoms).

The initial FCC samples were constructed by randomly-filling sites with Co, Cu, Fe, Ni, and X (Pd or Ti) atoms at the equiatomic compositions. To obtain the energetically-favorable HEA atomic configuration, atomic-swap operations (*i.e.*, MC attempts) were performed on randomly-chosen pairs of atoms of different types (10 distinct pairs) at a temperature of 300K. The acceptance of each MC attempt was determined according to the Metropolis criterion [48]. If the total energy of the system, $f$, at the step, $i+1$, is lower than that at the previous step, $i$, the atomic swap, $i+1$, is accepted. Otherwise, the acceptance probability, $P$, is calculated as:

$$P = e^{\frac{f(i+1)-f(i)}{kT}} \tag{1}$$

where $k$ is the Boltzmann constant, and $T$ is temperature. A uniform random number, $R$, $\in (0,1]$ is generated; if $R \leq P$, then the atomic swap is accepted. Otherwise, it is rejected. During each iteration loop, 100 successful MC attempts were performed. Then the energy was minimized (conjugate gradient) with respect to the atomic position (up to 100 relaxation steps). We also tested other iteration loops with different MC attempts and relaxation steps, and found that 100 MC attempts + 100 relaxation steps are not only efficient to obtain energetically-favorable configurations but also reasonable for the computational cost. This atomic and compositional relaxation process was terminated after 3.5-million iterations (including both atomic swaps and energy minimizations). The system energy was considered to be converged since the potential energy decreases by less than 0.02% in the final 1-million steps. The cohesive energies of all 36 A-B (and A-A) binary combinations of {Co, Cu, Fe, Ni, Pd, and Ti} in the $AB_3$ $L1_2$ unit cells were determined to compare with DFT calculations and to characterize the chemical affinity of each pair of atoms. The cohesive energies in the AB $B1$ unit cells were also calculated to verify the usage of the $L1_2$ structure to calculate the cohesive energy and characterize the chemical affinity.

Following relaxation of the CoCuFeNiPd and CoCuFeNiTi HEAs via 3.5-million MC swap/MD relaxation iterations followed by zero pressure equilibration at 300K for 0.2 ns, both samples were subjected to a uniaxial tensile stress at a strain rate of $1.0 \times 10^7$ $s^{-1}$ for 1.0 ns at 300K (a 1 fs time step was employed within an NPT ensemble). All MD and MC simulations were performed with periodic boundary conditions in all three $\langle 001 \rangle$ directions. The visualization software, OVITO [49], was utilized to analyze these simulation results.

The special quasi-random structure (SQS) approach is a useful tool to generate structures with specified correlations and is often employed specifically to generate random alloys [50,51]. Compared with hybrid MC and MD simulations, the SQS approach is more computationally efficient and can generate optimally-random solid solution in a finite simulation cell [52]. However, HEAs are often not random, exhibiting short-range ordering and/or atomic clustering – the extent of which depends on composition and temperature [16,19]. For such non-random structures, for which the nature of the short range order is to be determined (rather than assumed), hybrid MC and MD simulations are preferable to the SQS approach – provided that they are computationally feasible.

To describe the degree of atomic segregation, we characterized the SRO using the WCP for several nearest neighbour shells [53,54]:

$$WC_i(AB) = 1 - Z_i(AB)/[\chi(B)Z_i(A)] \tag{2}$$

where $Z_i(AB)$ is the number of B-type atoms around A-type atoms in the $i^{th}$ nearest neighbour shell, $Z_i(A)$ is the total number of atoms around A-type atoms in the $i^{th}$ nearest neighbour shell, and $\chi(B)$ is the atomic fraction of B-type atoms in the HEA. If $WC_i(AB) = 0$, the neighbouring AB pairs are randomly distributed, and there is no SRO. If $WC_i(AB) < 0$, chemical bonding between A- and B-type atoms is more favourable than random, while if $WC_i(AB) > 0$, AB bonds are less favourable than average. Therefore, WCP is related to the chemical affinity among constituent elements in HEAs.

### 2.2. DFT calculations

To evaluate the reliability of the interatomic potentials employed in the atomistic simulations, we used DFT calculations to determine the cohesive energy of all A-B (and A-A) elemental pairs in a binary $L1_2$ $AB_3$ alloy for all 36 A-B (and A-A) binary combinations of {Co, Cu, Fe, Ni, Pd, and Ti}. To characterize the chemical affinity in the CoCrFeNiPd and CoCrFeNiMn HEAs synthesized by Ding et al. [16], DFT calculations on the cohesive energies of $L1_2$ unit cells for the experimental CoCrFeNiPd and CoCrFeNiMn HEAs were also performed (binary combinations of {Co, Cr, Fe, Ni, Pd, and Mn}). The DFT calculations were performed, using the Vienna ab initio simulation package (VASP) [55] with a plane-wave basis and projector augmented wave (PAW) potentials [56,57]. The Perdew, Burke, and Ernzerhof (PBE) exchange correlation energy functional within the generalized gradient approximation (GGA) was employed [58]. For the binary-alloy, $L1_2$ $AB_3$, reference system, the cohesive energy is:

$$E_c(AB_3) = \frac{1}{4}[E_g(A) + 3E_g(B) - E_b(AB_3)] \tag{3}$$

where $E_b(AB_3)$ is the energy of the fully-relaxed $AB_3$ structure, and $E_g(A)$ and $E_g(B)$ are the energies of isolated A and B atoms in their ground state, respectively.

To compute the ground-state energies of the symmetry-broken spin polarized magnetic ground state of an isolated atom, DFT calculations were performed for a single atom in a large cubicle cell (14 Å × 14 Å × 14 Å) with periodic boundary conditions (PBCs) to avoid interactions with its periodic images. The convergence tolerance for the electronic self-consistency was set at $10^{-8}$ eV, and the plane-wave energy cutoff was 800 eV. The bulk energies of the $AB_3$ $L1_2$ alloy were calculated by fully-relaxing the ions and periodic cell lattice parameters to the electronic self-consistency with a tolerance of $10^{-8}$ eV and a force convergence tolerance of $10^{-4}$ eV/Å. A plane-wave energy cutoff of 520 eV and k point mesh of $15 \times 15 \times 15$ per cell were applied for all calculations.

## 3. Results

### 3.1. Atomic configurations before/after atomic swaps and energy minimizations

We focus on two, 5-element HEAs; four elements are common to both HEAs and were chosen to be of similar atomic sizes and electronegativities (i.e., Co, Cu, Fe, and Ni, see Fig. 1). The atomic sizes are calculated according to the fitted lattice constants of the interatomic potentials [43,44], and the electronegativities using the Allen scale were obtained from literature [59]. The average atomic size and electronegativity of these four elements are 1.25 Å and 1.84, respectively. The fifth element was chosen to have a greater atomic size and electronegativity difference (i.e., X = Pd or Ti, see

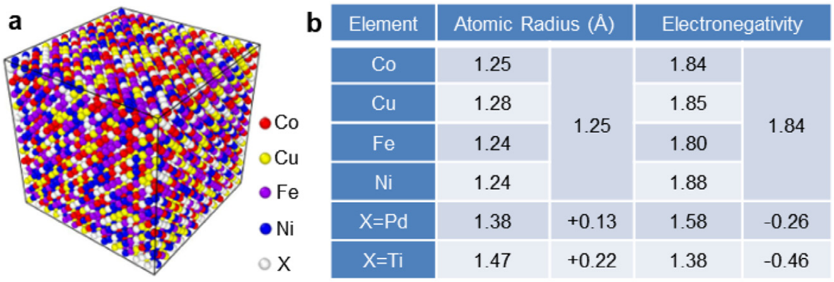

| Element | Atomic Radius (Å) | | Electronegativity | |
|---|---|---|---|---|
| Co | 1.25 | 1.25 | 1.84 | 1.84 |
| Cu | 1.28 | | 1.85 | |
| Fe | 1.24 | | 1.80 | |
| Ni | 1.24 | | 1.88 | |
| X=Pd | 1.38 | +0.13 | 1.58 | -0.26 |
| X=Ti | 1.47 | +0.22 | 1.38 | -0.46 |

**Fig. 1.** (a) Initial atomic configuration of CoCuFeNiX (X = Pd or Ti) with random elemental distributions. (b) Atomic radii and electronegativities of Co, Cu, Fe, Ni, Pd, and Ti. The numbers to the right of the entries for the four common elements are the means, and the values for the X elements are differences with respect to these means.

Fig. 1b). The relative differences between the atomic size and electronegativity of Pd and the average atomic size and electronegativity of the four elements are +0.13 Å and -0.26, while those between Ti and the four elements are +0.22 Å and -0.46. Hence, the relative differences for Ti are larger than those for Pd. Following Ding et al.'s suggestions [16], CoCuFeNiTi should exhibit stronger atomic segregation and SRO than CoCuFeNiPd because of the greater atomic size and electronegativity mismatch for Ti. Single-crystal FCC CoCuFeNiX (X = Pd or Ti) models with random elemental distributions were prepared (see Fig. 1a) for subsequent MC swapping and MD relaxation.

The variations of the potential energies for CoCuFeNiPd and CoCuFeNiTi HEAs with iteration steps during atomic swaps and energy minimizations are shown in Fig. 2a. The results in Fig. 2a demonstrate that the potential energy of the CoCuFeNiPd HEA converges to -4.11 eV/atom after 2.5-million iteration steps, and that of the CoCuFeNiTi HEA converges to -4.43 eV/atom after 2.5-million iteration steps. The evolutions of the atomic configurations for CoCuFeNiPd and CoCuFeNiTi HEAs during the iterations are presented in Movies S1 and S2 in the Supplementary Materials, respectively. Initially, the atomic configuration is purely random, and all WCPs are zero (see Figs. S1 in the Supplementary Materials). The atomic configuration of the CoCuFeNiPd HEA after 3.5-million atomic swaps and energy minimizations is exhibited in Fig. 2b, clearly showing the formation of atomic clustering and SRO. Clustering of Co, Cu, and Ni is particularly obvious while Fe and Pd appear in a mutual solution. The atomic configuration of the CoCuFeNiTi HEA after 3.5-million atomic swaps and energy minimizations is plotted in Fig. 2c. A comparison of the atomic configurations in the CoCuFeNiPd (Fig. 2b) and CoCuFeNiTi (Fig. 2c) HEAs indicates that the overall tendency for clustering is much reduced upon replacing Pd with Ti.

For the CoCuFeNiPd HEA, the WCPs for the 1st nearest neighbour shell, $WC_1$, are shown in Fig. 2d for all elemental pairs, where negative values indicate favourable atomic pairs. These data show that compared to the random configuration ($WC_1 = 0$), there is a strong tendency to form Cu-Cu ($WC_1 = -1.54$), Ni-Ni ($WC_1 = -1.46$), and Co-Co ($WC_1 = -1.13$) pairs and, to a lesser extent, Pd-Pd pairs ($WC_1 = -0.71$), consistent with the cluster-formation conclusions drawn from the observation of the atomic configuration (Fig. 2b). There is also a strong tendency for Pd-Fe ($WC_1 = -0.67$) bond formation and a weaker tendency for the Ni-Co ($WC_1 = -0.14$) bond formation. Moreover, there is a strong tendency for Pd and Ni to avoid each other. Fig. 2e and 2f show the WCPs for the 1st to 13th nearest neighbour shell, $WC_n$, of pairs formed with Co and Cu, respectively. Figures S2a, S2b, and S2c in the Supplementary Materials present the $WC_n$ of pairs formed with Fe, Ni, and Pd, respectively. These data indicate that while the strength of the tendency to have particular neighbour elements decays with the distance, the decay is monotonic; i.e., we see no tendency for long-range chemical ordering, in the sense of ordered compound formation. We note that the distance of the 13th nearest neighbour shell of an atom is only ~ 0.92 nm, which is less than one fifth of the linear dimension of the simulation cell (4.68 nm). This trend suggests that the effects of the periodic boundary conditions on the reported WCP results are negligible.

For the CoCuFeNiTi HEA, the WCPs for the 1st nearest neighbour shell, $WC_1$, are shown in Fig. 2g for all elemental pairs. Fig. 2h and 2i exhibit the WCPs for the 1st to 13th nearest neighbour shell, $WC_n$, of pairs formed with Co and Cu, respectively. Figures S2d, S2e, and S2f present $WC_n$ of pairs formed with Fe, Ni, and Pd, respectively. Compared with the WCPs for the CoCuFeNiPd HEA, the overall magnitude of the SRO is smaller by replacing Pd with Ti. Nonetheless, most of the SRO tendencies are the same. Like Pd, Ti favors bonds with Fe. However, Ti is relatively indifferent to all other types of bonds (whereas Pd avoids forming bonds with Ni and Co). We note that the relative differences in the atomic size and electronegativity for Ti with respect to the other four elements (Co, Cu, Fe, and Ni) are larger than those of Pd. If the differences in the atomic size and electronegativity were the only origin for the atomic segregation and cluster formation, we should expect that the SRO in the Ti-containing HEA should be larger than that in the Pd-containing HEA. Clearly this trend is not the case. This feature is even clearer in Figs. 2h and 2i where we see that the overall magnitudes of the $WC_n$ in the Ti-containing HEA are much smaller than in the corresponding data for the Pd-containing HEA in Figs. 2e and 2f. Clearly, the reduction in the atomic clustering and SRO on substituting Ti for Pd in the HEA is not associated solely with differences in the atomic size and electronegativity.

### 3.2. Elemental distribution after atomic swaps and energy minimizations

To further quantify the elemental distribution in the CoCuFeNiPd HEA, detailed analyses of the atomic fraction and position of each constituent element (Co, Cu, Fe, Ni, and Pd) were performed. The atomic configuration of the CoCuFeNiPd HEA after 3.5-million atomic swaps and energy minimizations is presented in Fig. 3a (same as Fig. 2b). Spatial variations of the atomic fractions of Co, Cu, Fe, Ni, and Pd (from the left to right in the shaded band marked "b" in Fig. 3a) are plotted in Fig. 3b. These data demonstrate that Cu and Pd atoms are found in a greater proportion in the left region (0 to ~ 1.5 nm), Ni and Co atoms are clustered in the middle region (~ 1.5 to ~ 3.5 nm), while Cu, Fe, and Pd atoms dominate the right region (~ 3.5 to ~ 4.5 nm), further confirming the strong SRO (Cu-Cu, Ni-Ni, Co-Ni, and Fe-Pd pairs) in the CoCuFeNiPd HEA. Atomic distributions of Fe and Cu atoms in the shaded band marked "c" in Fig. 3a are shown in Fig. 3c. The top image in Fig. 3c demonstrates that Fe atoms tend to form nearest-neighbor pairs and that these pairs are distributed more or less randomly throughout the simulation cell. While large clusters of Cu atoms form (see the bottom image of Fig. 3c), no such large clusters of Fe atoms occur. The WCPs of Fe-Fe and Cu-Cu are -0.62 and -1.54 (Fig. 2d), respectively, confirming the

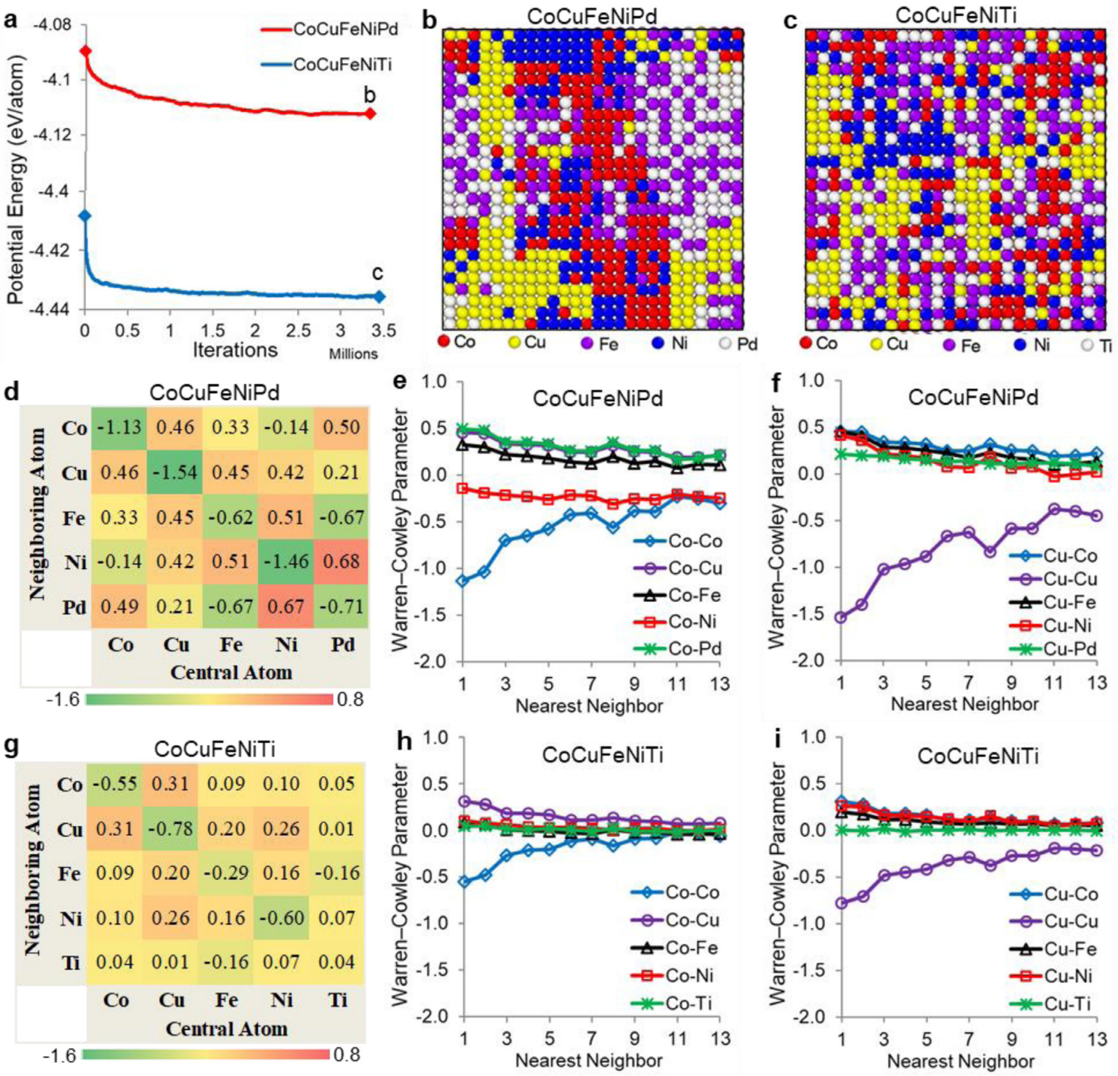

**Fig. 2.** (a) Variations of potential energies of CoCuFeNiPd and CoCuFeNiTi HEAs with iteration steps. Atomic configurations in a {001} cut through the FCC HEA simulation cell of (b) CoCuFeNiPd and (c) CoCuFeNiTi. (d) Warren-Cowley parameters for the 1st nearest neighbour shell, $WC_1$, of all elemental pairs in the CoCuFeNiPd HEA. Warren-Cowley parameters for the 1st to 13th nearest neighbour shells, $WC_n$, around (e) Co atoms and (f) Cu atoms in the CoCuFeNiPd HEA. (g-i) Panels are the same as (d-f), but for the CoCuFeNiTi HEA.

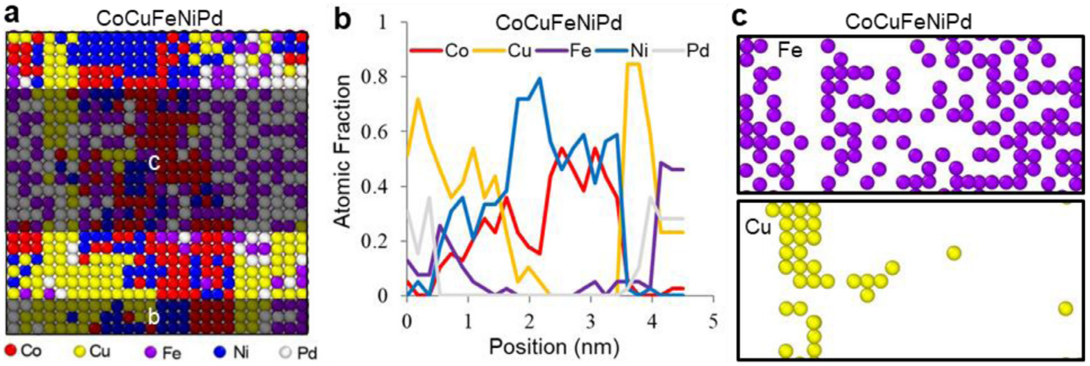

**Fig. 3.** (a) Atomic configuration in a {001} cut through the CoCuFeNiPd HEA after 3.5-million iteration steps (same as Fig. 2b). (b) Variation of atomic fractions for constituent elements (Co, Cu, Fe, Ni, and Pd) in the shaded region "b" in (a). (c) Spatial arrangements of Fe and Cu atoms in the shaded region "c" in (a).

**Table 1**
Comparison of cohesive energies of the $L1_2$ unit cell between (a) MD simulations and (b) DFT calculations.

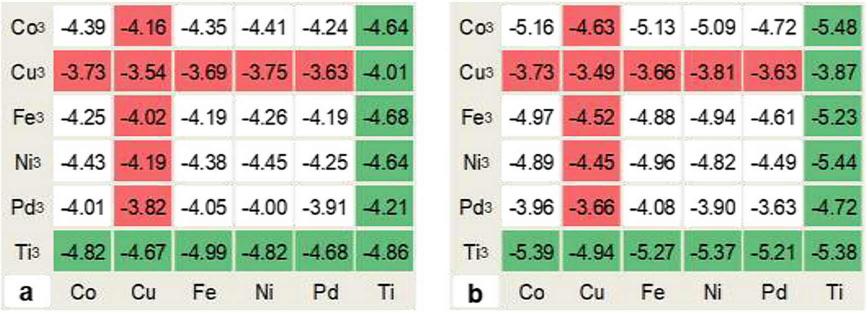

| a | Co | Cu | Fe | Ni | Pd | Ti |
|---|---|---|---|---|---|---|
| $Co_3$ | -4.39 | -4.16 | -4.35 | -4.41 | -4.24 | -4.64 |
| $Cu_3$ | -3.73 | -3.54 | -3.69 | -3.75 | -3.63 | -4.01 |
| $Fe_3$ | -4.25 | -4.02 | -4.19 | -4.26 | -4.19 | -4.68 |
| $Ni_3$ | -4.43 | -4.19 | -4.38 | -4.45 | -4.25 | -4.64 |
| $Pd_3$ | -4.01 | -3.82 | -4.05 | -4.00 | -3.91 | -4.21 |
| $Ti_3$ | -4.82 | -4.67 | -4.99 | -4.82 | -4.68 | -4.86 |

| b | Co | Cu | Fe | Ni | Pd | Ti |
|---|---|---|---|---|---|---|
| $Co_3$ | -5.16 | -4.63 | -5.13 | -5.09 | -4.72 | -5.48 |
| $Cu_3$ | -3.73 | -3.49 | -3.66 | -3.81 | -3.63 | -3.87 |
| $Fe_3$ | -4.97 | -4.52 | -4.88 | -4.94 | -4.61 | -5.23 |
| $Ni_3$ | -4.89 | -4.45 | -4.96 | -4.82 | -4.49 | -5.44 |
| $Pd_3$ | -3.96 | -3.66 | -4.08 | -3.90 | -3.63 | -4.72 |
| $Ti_3$ | -5.39 | -4.94 | -5.27 | -5.37 | -5.21 | -5.38 |

strong clustering tendency for Cu atoms and the much weaker tendency for Fe-atom clusters in the CoCuFeNiPd HEA.

### 3.3. Cohesive energy and chemical affinity of binary combinations

In order to understand the observed tendencies for SRO in the HEAs, we examine the cohesive energies for all 36 A-B binary combinations of {Co, Cu, Fe, Ni, Pd, and Ti} in the $AB_3$ $L1_2$ intermetallic crystal structure. The cohesive energies of the $AB_3$ $L1_2$ structures, as determined from the interatomic potentials used in MD ($E_{MD}$) and DFT ($E_{DFT}$), are listed in Table 1. The relative errors between these cohesive energies (i.e., $|E_{MD}$ - $E_{DFT}|$ / $E_{DFT}$) are shown in Table S2. The cohesive energies from the DFT calculations range from -5.48 to -3.49 eV while their differences with respect to those determined using the MD interatomic potentials range from -0.28 to 0.84 eV with an average error of ~8%. While the DFT and MD interatomic potential-based cohesive energies do not show perfect agreement (as expected), the MD interatomic potentials are remarkably successful in reproducing the most important trends. For example, both results indicate that the Cu-Cu pairs exhibit the highest cohesive energy (i.e., A = Cu, B = Cu), Cu-containing pairs (shaded in red) always have higher cohesive energies than other pairs, and Ti-containing pairs (shaded in green) always have lower cohesive energies than other pairs. Both DFT and interatomic potential calculations show that atomic pairs consisting of Co, Fe, Ni, and Pd atoms are of low energy. When Pd is replaced by Ti (i.e., X = Ti), the cohesive energies of the Cu-X pair decrease (the cohesive energies of Cu-Ti pairs are lower than those of Cu-Pd) and are comparable to the Co, Fe, and Ni pairs in DFT. The consistency in the calculated cohesive energies between DFT and the interatomic potentials provides strong evidence that the main trends obtained from the MC swapping and MD relaxations are reliable.

Using the absolute values of cohesive energies in Table 1a, we also calculate normalized cohesive energy values in the CoCuFeNiPd and CoCuFeNiTi HEAs as,

$$E_n(AB_3) = [E_h - E_c(AB_3)]/(E_h - E_l) \tag{4}$$

where $E_c(AB_3)$ is the cohesive energy of an $AB_3$ unit cell determined from the interatomic potentials, $E_h$ is the highest value of $E_c(AB_3)$, and $E_l$ is the lowest value of $E_c(AB_3)$. The normalized cohesive energies for an $AB_3$ unit cell in the CoCuFeNiPd and CoCuFeNiTi HEAs are presented in Tables S1a and S1b in the Supplementary Materials, respectively. As described above, we can also evaluate the chemical affinity of atomic pairs in terms of the normalized cohesive energy (i.e., high/low cohesive energy indicates weak/strong chemical affinity). We define the chemical affinities (*CA*) of elemental pairs as,

$$CA(AB) = [E_n(AB_3) + E_n(BA_3)]/2 \tag{5}$$

where $E_n(AB_3)$ and $E_n(BA_3)$ are the normalized cohesive energies of $AB_3$ and $BA_3$ unit cells, respectively. The chemical affinities for elemental pairs in the CoCuFeNiPd and CoCuFeNiTi HEAs are presented in Tables 2a and 2b, respectively (strong/weak affinity is shaded in green/red).

Considering the elemental pairs in the CoCuFeNiPd HEA, we see that the chemical affinities of Ni-Ni ($CA$ = 1.00), Co-Ni ($CA$ = 0.97), and Co-Co ($CA$ = 0.94) are very high (see Table 2a), contributing to the formation of SRO between Co and Ni. The negative values of WCPs in Fig. 2d (i.e., Ni-Ni: $WC_1$ = -1.46, Co-Ni: $WC_1$ = -0.14, and Co-Co: $WC_1$ = -1.13) confirm the dominant presence of Ni-Ni, Co-Ni, and Co-Co pairs. Even though the chemical affinity of Ni-Fe is strong ($CA$ = 0.86), it is still weaker than the chemical affinities of Ni-Ni ($CA$ = 1.00), Co-Ni ($CA$ = 0.97), and Co-Co ($CA$ = 0.94), inhibiting the formation of SRO between Ni and Fe. Since the formation of short range order involves site competition, very strong chemical affinity can prevent strong correlations from forming between pairs where merely strong affinity exists. These features clearly demonstrate that the strong chemical-affinity disparity drives the atomic segregation, SRO, and cluster formation. Besides Co and Ni atoms, the chemical affinities of Fe-Fe ($CA$ = 0.72), Pd-Fe ($CA$ = 0.64), and Pd-Pd ($CA$ = 0.41) are stronger than other pairs among Pd, Fe, and Cu atoms. The negative values of WCPs in Fig. 2d, that is, Pd-Fe ($WC_1$ = -0.67), Pd-Pd ($WC_1$ = -0.71), and Fe-Fe ($WC_1$ = -0.62) verify the formation of these atomic pairs, further confirming that the strong-chemical-affinity disparities drive the formation of atomic pairs.

It is noted that the WCP of the Cu-Cu pair in Fig. 2d is also negative ($WC_1$ = -1.54), indicating that Cu-Cu pairs also form atomic clusters in the CoCuFeNiPd HEA. Moreover, Cu-Cu atomic clusters are also observed in the left and right bottom regions in Fig. 2b. However, Table 1 lists that Cu-Cu pairs have the highest cohesive energy among all elemental pairs. Therefore, apart from the low-energy clusters (such as Ni-Ni, Co-Ni, and Co-Co) and medium-energy clusters (such as Fe-Fe, Pd-Fe, and Pd-Pd), surprisingly, high-energy Cu-Cu clusters are also formed in the CoCuFeNiPd HEA. Currently, the formation of high-energy clusters remains unclear. However, from the chemical-affinity disparities among different atomic pairs, we are able to explain the origin of their formation. The formation of atomic pairs with strong chemical affinity drives the formation of low-energy clusters to minimize the energy of the whole system. Nevertheless, these low- and medium-energy clusters (Ni-Ni, Co-Ni, Co-Co, Fe-Fe, Fe-Pd, and Pd-Pd pairs) do not include Cu atoms. Consequently, Cu atoms must bond with themselves despite the formation of high-energy clusters. Since the energy reduction in forming the low- and medium-energy clusters offsets the energy increase in forming the high-energy clusters, the overall system energy is reduced.

In the CoCuFeNiTi HEA, we see that the chemical affinity of Fe-Ti ($CA$ = 0.89) is high (Table 2b), contributing to the formation of SRO between Fe and Ti. The negative value of WCP in Fig. 2g (i.e., Fe-Ti: $WC_1$ = -0.16) confirms the presence of Fe-Ti pairs. Be-

**Table 2**
Chemical affinity of elemental pairs for (a) CoCuFeNiPd and (b) CoCuFeNiTi based upon the MD data in Table 1.

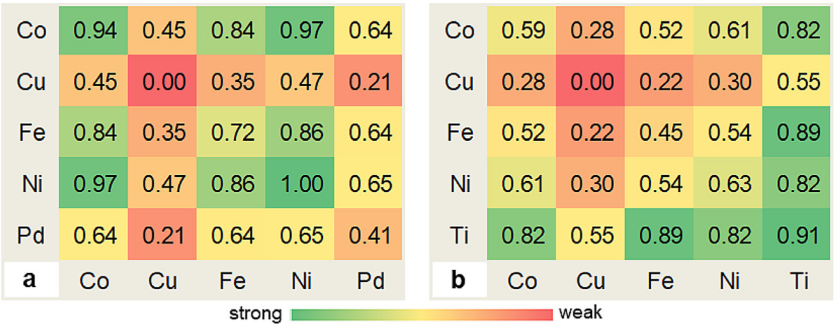

|  |  |  |  |  |  |
|---|---|---|---|---|---|
| Co | 0.94 | 0.45 | 0.84 | 0.97 | 0.64 |
| Cu | 0.45 | 0.00 | 0.35 | 0.47 | 0.21 |
| Fe | 0.84 | 0.35 | 0.72 | 0.86 | 0.64 |
| Ni | 0.97 | 0.47 | 0.86 | 1.00 | 0.65 |
| Pd | 0.64 | 0.21 | 0.64 | 0.65 | 0.41 |
| **a** | Co | Cu | Fe | Ni | Pd |

|  |  |  |  |  |  |
|---|---|---|---|---|---|
| Co | 0.59 | 0.28 | 0.52 | 0.61 | 0.82 |
| Cu | 0.28 | 0.00 | 0.22 | 0.30 | 0.55 |
| Fe | 0.52 | 0.22 | 0.45 | 0.54 | 0.89 |
| Ni | 0.61 | 0.30 | 0.54 | 0.63 | 0.82 |
| Ti | 0.82 | 0.55 | 0.89 | 0.82 | 0.91 |
| **b** | Co | Cu | Fe | Ni | Ti |

sides Fe and Ti atoms, the chemical affinities of Ni-Ni ($CA = 0.63$), Co-Ni ($CA = 0.61$), and Co-Co ($CA = 0.59$) are stronger than other pairs among Co, Ni, and Cu atoms. The negative values of WCPs in Fig. 2g also verify that Ni-Ni ($WC_1$ = -0.60) and Co-Co ($WC_1$ = -0.55) pairs are formed. However, the overall magnitudes of the SRO in the CoCuFeNiTi HEA are smaller than that in the CoCuFeNiPd HEA. The underlying reason is that the chemical affinity of Fe-Fe ($CA = 0.45$) is not sufficiently strong to lead to a large amount of Ti-Fe atomic cluster even though the chemical affinities of Ti-Ti ($CA = 0.91$) and Fe-Ti ($CA = 0.89$) are quite strong. Moreover, Ti also has strong chemical affinities with Co ($CA = 0.82$) and Ni ($CA = 0.82$), which are comparable to Fe ($CA = 0.89$) and Ti ($CA = 0.91$), weakening the formations of Co-Co and Ni-Ni pairs. However, in the CoCuFeNiPd HEA, the chemical affinities of all atomic pairs between Ni and Co (*i.e.*, Ni-Ni: $CA = 1.00$, Co-Ni: $CA = 0.97$, and Co-Co: $CA = 0.94$) are sufficiently high, contributing to the larger amount of Co-Ni atomic clusters and higher magnitudes of the SRO than the CoCuFeNiTi HEA. The negative value of Cu-Cu: $WC_1$ = -0.78 also indicates the formation of high-energy Cu-Cu clusters, although weaker than in the CoCuFeNiPd HEA. Such weakening is due to the relatively-strong chemical affinity of Cu-Ti ($CA = 0.55$).

An interesting observation is that the average lattice constant of the CoCuFeNiPd HEA is 3.65 Å, which is obtained after 2.5-million iteration steps. The average lattice constant of atomic pairs ($AB_3$) in the CoCuFeNiPd HEA that was used to obtain the cohesive energies in Table 1a is 3.63 Å, which agrees well with the average lattice constant of the CoCuFeNiPd HEA. This trend indicates that all the atomic pairs tend to lower their cohesive-energy states by adopting close to the most energetically-favorable lattice constants. Hence, the competitions and compromises of these atomic pairs will eventually determine the overall system energy. This argument further highlights the importance of chemical-affinity disparity in driving the atomic segregation, SRO, and cluster formation in HEAs. The stress-strain curves as generated from tensile deformations of CoCuFeNiPd and CoCuFeNiTi HEAs (equilibrated through 3.5-million MC swap/MD relaxation iterations) are shown in Fig. S3. Clearly, the HEA that displayed more pronounced atomic segregation and short-range ordering (CoCuFeNiPd) has a higher strength than the HEA with low short-range ordering (CoCuFeNiTi), in agreement with the conclusions of Ding et al. [16].

## 4. Discussion

### 4.1. Experimental observation of high-energy Cu-Cu clusters

Interestingly, Xu et al. [37] also revealed nanoscale phase separation in the single-phase FCC $Al_{0.5}CoCrCuFeNi$ HEA, using scanning transmission electron microscopy (STEM) combined with atom probe tomography (APT), and found two distinct domains: one is the FCC structure enriched with Cu, and the other is an $L1_2$ structure with Fe, Cr, Co, and Ni. Moreover, the distribution of Al was shown to be uniform. Similarly, Santodonato et al. [41] also observed Cu-rich precipitates in the $Al_xCoCrCuFeNi$ HEA system by high-resolution scanning electron microscopy (SEM). Hence, Xu et al.'s [37] and Santodonato et al.'s [41] experimental observations provide the direct evidence to support the existence of high-energy clusters in HEAs. We note, however, Xu et al. [37] attributed the nanoscale phase separation to the Al addition and atomic-size differences, which was based on the reason that their measured radius of Al (0.143 nm) is larger than those of other constituent elements (Fe: 0.128 nm; Ni: 0.128 nm; Co: 0.128 nm; Cu: 0.127 nm; and Cr: 0.130 nm). Thus, the nanoscale coherent phase separation can eliminate the lattice strains caused by the atomic-size differences of the constituent components. Here, our simulations suggest that the nanoscale atomic segregation can be attributed to the chemical-affinity disparity, highlighting the importance of chemical affinity in the nanoscale coherent phase separation and the origin of the formation of high-energy clusters in HEAs.

### 4.2. Effect of chemical affinity on atomic segregation and SRO

Fig. 4 schematically illustrates the relationship amongst the chemical-affinity disparity, exclusivity in the chemical composition, SRO, atomic segregation, and cluster formation in these two HEAs. In general, we are able to divide the chemical affinity of constituent elemental pairs (in Fig. 4ai) into three classes, that is, a strong-chemical-affinity class (SCAC) ($0.75 < CA \leq 1.0$), a medium-chemical-affinity class (MCAC) ($0.35 \leq CA \leq 0.75$), and a weak-chemical-affinity class (WCAC) ($0 \leq CA < 0.35$). For the CoCuFeNiPd HEA, the Co-Co, Co-Ni, and Ni-Ni pairs belong to SCAC, the Fe-Fe, Fe-Pd, and Pd-Pd pairs belong to MCAC, while Cu-Cu belongs to WCAC, as shown in Fig. 4aii. For this HEA, the chemical elements in the three classes are mutually exclusive, that is, there is no overlap of chemical elements amongst the three classes (i.e., high exclusivity in chemical compositions). As a result, the formed clusters tend to avoid overlap or interpenetration. Hence, due to the large chemical-affinity disparity and the mutual exclusion of chemical elements in the three classes, the CoCuFeNiPd HEA shows strong SRO, atomic segregation, and cluster formation as illustrated in Fig. 4aiii. For the CoCuFeNiTi HEA (in Fig. 4bi), the Ti-Ti, Ti-Fe, Ti-Ni, and Ti-Co pairs belong to the SCAC, the Ni-Ni, Co-Ni, Co-Co, Cu-Ti, Fe-Ni, Co-Fe, and Fe-Fe pairs belong to MCAC, while Cu-Cu pair belongs to WCAC, as presented in Fig. 4bii. It is seen that there is low exclusivity of chemical elements amongst the three classes, that is, there are overlaps between SCAC and MCAC (that is, Ti, Fe, Ni, and Co) and between MCAC and WCAC (that is, Cu). The overlaps of chemical elements between classes result in large atomic-

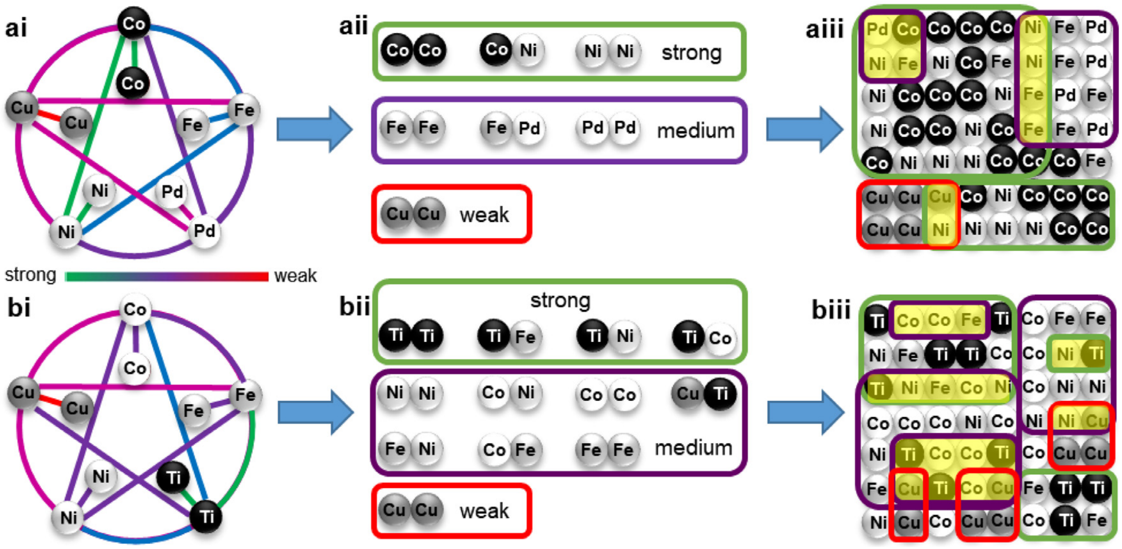

**Fig. 4.** Large disparity in chemical affinities (ai), high exclusivity in chemical compositions (aii), and strong SRO and clustering (aiii) in the CoCuFeNiPd HEA. Large disparity in chemical affinities (bi) and low exclusivity in chemical compositions (bii) and weak SRO and clustering (biii) in the CoCuFeNiTi HEA. The color of the connecting lines between two atoms in (ai) and (bi) represents the chemical-affinity magnitude. Atom gray-levels distinguish atom type, *i.e.*, from the minimum (black) to maximum (white) grey level: (aii) Co, Cu, Fe, Ni, and Pd; (bii) Ti, Cu, Fe, Ni, and Co. Overlap/interpenetration between different-chemical-affinity clusters are shaded in yellow in (aiii) and (biii).

cluster interpenetrations (shaded in yellow in Fig. 4biii) and the weakening of atomic segregation and SRO.

To explore whether chemical-affinity disparity and exclusivity can account for the observed atomic segregation and short-range ordering in the CoCrFeNiPd and CoCrFeNiMn HEAs synthesized by Ding et al. [16], DFT calculations on the cohesive energies of $L1_2$ unit cells for the experimental CoCrFeNiPd and CoCrFeNiMn HEAs were also performed (see Table S3). The chemical affinities of elemental pairs in the experimental CoCrFeNiPd and CoCrFeNiMn HEAs were also determined based upon these cohesive energies and are reported in Table S4. The results in Tables S3 and S4 indicate that the cohesive energies of the unit cells and chemical affinities of elemental pairs in the CoCrFeNiPd HEA are similar to those in the CoCrFeNiMn HEA. Therefore, chemical-affinity disparity and exclusivity do not provide a full description of the atomic segregation and short-range ordering in experimental CoCrFeNiPd and CoCrFeNiMn HEAs, while the atomic-size and electronegativity differences [16] and misfit volume [60] may dominate. However, our results show that the CoCuFeNiPd HEA exhibits much stronger atomic segregation and short-range ordering than the CoCuFeNiTi HEA, despite the larger differences in the relative atomic size and electronegativity of Ti with other constituent elements, as compared to those of Pd, suggesting that the previously proposed atomic-size, electronegativity differences and misfit volume are insufficient indicators to explain the atomic segregation and short-range ordering in our CoCuFeNiPd and CoCuFeNiTi HEAs. Indeed, this is what led to our in-depth analyses and proposal of chemical-affinity disparity and exclusivity to explain the atomic segregation and SRO in these HEAs.

### 4.3. Chemical affinities characterized using L12 and B1 structures

In order to investigate the degree to which our choice of $L1_2$ affects our conclusions regarding chemical affinities, we performed an additional set of MD calculations of cohesive energies and chemical affinities for the AB rock salt ($B1$) structure (see Table S5). These results using a B1 lattice show that Ni-Ni, Co-Ni, and Co-Co have the strongest chemical affinities in the CoCuFeNiPd HEA. Besides Co and Ni atoms, the chemical affinities of Fe-Fe, Pd-Fe, and Pd-Pd are stronger than other pairs among Pd, Fe, and Cu atoms, which belong to the medium-chemical-affinity class. The Cu-Cu pair has the weakest chemical affinity. Therefore, the strong-chemical-affinity, medium-chemical-affinity, and weak-chemical-affinity classes in the CoCuFeNiPd HEA determined using calculations of $B1$ structure are consistent with those obtained on the basis of the $L1_2$ structure. For the CoCuFeNiTi HEA, the Ti has strong chemical affinities with Co, Fe, Ni, and Ti (associated pairs belong to the strong-chemical-affinity class). Ti-Cu, Ni-Ni, Co-Ni, and Co-Co are medium-chemical-affinity pairs, while Cu-Cu is a low-chemical-affinity pair. The chemical affinities calculated from the $B1$ structures also demonstrate that there is low exclusivity of chemical elements amongst the three classes in the CoCuFeNiTi HEA, resulting in large atomic-cluster interpenetrations and the weakening of atomic segregation and SRO.

Even though there are differences in the numerical values of chemical affinity between $AB_3$ $L1_2$ and AB $B1$ structures, the overall trends are consistent, verifying the usage of the $L1_2$ structure to calculate the cohesive energy and characterize the chemical affinity. The calculations of both structures support that the chemical-affinity disparity and exclusivity are the origin for the atomic segregation and short-range ordering in the CoCuFeNiPd and CoCuFeNiTi HEAs. Moreover, the average lattice constant of the $L1_2$ structure in the CoCuFeNiPd HEA is 3.63 Å, which is very close to the average lattice constant of the CoCuFeNiPd HEA (3.65 Å); this corresponds to a difference in atomic volume of only 1.6%. However, the average lattice constant of the $B1$ structure in the CoCuFeNiPd HEA (4.83Å) is 32% larger than that of the CoCuFeNiPd HEA (the discrepancy in the atomic volume is 132%). This consistency on the average lattice constant of the $L1_2$ structures, together with the similarity in atom composition in $L1_2$ and the HEA, further suggests that $L1_2$ is a reasonably good surrogate structure. The cohesive energies of $L1_2$ structures from DFT calculations are also comparable with the MD calculations, further confirming the choice of $L1_2$ structure and the reliability of the EAM potentials.

### 4.4. Design HEAs with excellent properties using chemical-affinity disparity and exclusivity

It was reported that the atomic segregation and SRO in a HEA was able to increase the resistance to dislocation motion, leading to an increase in the yield strength without compromising strain hardening and tensile ductility [16]. The underlying deformation mechanism differs markedly from those in the Cantor alloy and other FCC HEAs, whose elemental distributions are relatively-random and uniform, with no resistance to dislocation motion. Besides dislocation motion, SROs were also found to play an important role in twining and stress-induced phase transformation behaviors in HEAs [23]. The present study indicates that by selecting the constituent elements with large/small disparity in chemical affinities or high/low exclusivity in the chemical compositions, there is a great opportunity to tune the microstructures of HEAs to achieve specific mechanical properties. For example, suppose we would like to design a HEA with less atomic segregation and lower yield strength. In that case, we could choose constituent elements with a smaller disparity in chemical affinities or a larger disparity in chemical affinities but lower exclusivity in chemical compositions. On the other hand, to obtain a HEA with atomic segregation and SRO consisting of specific types of atoms, we should choose constituent elements with a large disparity in chemical affinities and high exclusivity in chemical elements in forming atomic clusters with different energy levels. Such designed HEAs may have a higher yield strength while retaining strain hardening and tensile ductility. Hence, the findings of the present study provide useful guidelines for designing HEAs with specific mechanical properties. It should be noted that the database for the chemical affinity and exclusivity of different atomic pairs could be constructed by performing MD simulations or DFT calculations.

## 5. Summary

In summary, we performed iterative MC and MD simulations to achieve the energetically-favourable atomic configurations of CoCuFeNiX (X = Pd or Ti) HEAs. In the energy-minimization loops, the MC simulation was used to realize atomic swaps while the MD simulation was employed to calculate the system energy. For the CoCuFeNiPd HEA, strong atomic segregation and SRO were observed. For the CoCuFeNiTi HEA, however, atomic segregation and SRO are much less pronounced than that observed in the CoCuFeNiPd HEA. We showed that differences in the atomic size and electronegativity were insufficient to account for variations of atomic segregation and SRO in these HEAs. Based on the cohesive energies between different atom pairs in these HEAs, we suggest that disparity in the chemical affinity and exclusivity of the chemical composition in forming atomic pairs drive atomic segregation, SRO, and formation of low- and high-energy clusters. Our DFT calculations also validated the atomic potentials in MD simulations, suggesting that the findings from the MD and MC simulations are reliable. The present study not only highlights the importance of the chemical-affinity disparity and exclusivity in governing the atomic segregation, SRO, and cluster formation in HEAs, but also provides useful guidelines for designing HEAs with desired mechanical properties for engineering applications.

## Declaration of Competing Interest

The authors declare that they have no known competing financial interests or personal relationships that could have appeared to influence the work reported in this paper.

## Acknowledgements

S. C., Z. H. A., Z. G. Y., and Y.-W. Z. gratefully acknowledge the financial support from the Agency for Science, Technology and Research (A*STAR) under grant AMDM A1898b0043, and the use of computing resources at the A*STAR Computational Resource Centre and National Supercomputer Centre, Singapore. S. P. and D. J. S. acknowledge the General Research of the Research Grant Council of Hong Kong SAR, China (CityU 11211019). P. K. L. very much appreciates the supports from (1) the U.S. Army Office Project (W911NF-13-1-0438 and W911NF-19-2-0049) with the program managers, Drs. Michael P. Bakas, David M. Stepp, and S. Mathaudhu, and (2) the National Science Foundation (DMR-1611180 and 1809640) with the program directors, Drs. Judith Yang, Gary Shiflet, and Diana Farkas.

## Supplementary materials

Supplementary material associated with this article can be found, in the online version, at doi:10.1016/j.actamat.2021.116638.

## References

[1] J.H. Martin, B.D. Yahata, J.M. Hundley, J.A. Mayer, T.A. Schaedler, T.M. Pollock, 3D printing of high-strength aluminium alloys, Nature 549 (2017) 365.

[2] Z. Wu, R. Ahmad, B. Yin, S. Sandlöbes, W.A. Curtin, Mechanistic origin and prediction of enhanced ductility in magnesium alloys, Science 359 (2018) 447–452.

[3] E. Alabort, D. Barba, M.R. Shagiev, M.A. Murzinova, R.M. Galeyev, O.R. Valiakhmetov, A.F. Aletdinov, R.C. Reed, Alloys-by-design: Application to titanium alloys for optimal superplasticity, Acta Mater 178 (2019) 275–287.

[4] J.-W. Yeh, S.-K. Chen, S.-J. Lin, J.-Y. Gan, T.-S. Chin, T.-T. Shun, C.-H. Tsau, S.-Y. Chang, Nanostructured high-entropy alloys with multiple principal elements: novel alloy design concepts and outcomes, Adv. Eng. Mater. 6 (2004) 299–303.

[5] B. Cantor, I.T.H. Chang, P. Knight, A.J.B. Vincent, Microstructural development in equiatomic multicomponent alloys, Mater. Sci. Eng. A 375 (2004) 213–218.

[6] J. Wang, S. Wu, S. Fu, S. Liu, M. Yan, Q. Lai, S. Lan, H. Hahn, T. Feng, Ultrahigh hardness with exceptional thermal stability of a nanocrystalline CoCrFeNiMn high-entropy alloy prepared by inert gas condensation, Scr. Mater. 187 (2020) 335–339.

[7] Z. Lei, X. Liu, Y. Wu, H. Wang, S. Jiang, S. Wang, X. Hui, Y. Wu, B. Gault, P. Kontis, D. Raabe, L. Gu, Q. Zhang, H. Chen, H. Wang, J. Liu, K. An, Q. Zeng, T.-G. Nieh, Z. Lu, Enhanced strength and ductility in a high-entropy alloy via ordered oxygen complexes, Nature 563 (2018) 546–550.

[8] Z. Li, K.G. Pradeep, Y. Deng, D. Raabe, C.C. Tasan, Metastable high-entropy dual-phase alloys overcome the strength-ductility trade-off, Nature 534 (2016) 227–230.

[9] E.P. George, W.A. Curtin, C.C. Tasan, High entropy alloys: A focused review of mechanical properties and deformation mechanisms, Acta Mater 188 (2020) 435–474.

[10] M. Naeem, H. He, S. Harjo, T. Kawasaki, F. Zhang, B. Wang, S. Lan, Z. Wu, Y. Wu, Z. Lu, C.T. Liu, X.-L. Wang, Extremely high dislocation density and deformation pathway of CrMnFeCoNi high entropy alloy at ultralow temperature, Scr. Mater. 188 (2020) 21–25.

[11] C. Varvenne, A. Luque, W.A. Curtin, Theory of strengthening in fcc high entropy alloys, Acta Mater 118 (2016) 164–176.

[12] Y. Yao, Z. Huang, P. Xie, S.D. Lacey, R.J. Jacob, H. Xie, F. Chen, A. Nie, T. Pu, M. Rehwoldt, D. Yu, M.R. Zachariah, C. Wang, R. Shahbazian-Yassar, J. Li, L. Hu, Carbothermal shock synthesis of high-entropy-alloy nanoparticles, Science 359 (2018) 1489–1494.

[13] G. Laplanche, S. Berglund, C. Reinhart, A. Kostka, F. Fox, E.P. George, Phase stability and kinetics of $\sigma$-phase precipitation in CrMnFeCoNi high-entropy alloys, Acta Mater 161 (2018) 338–351.

[14] F. Otto, Y. Yang, H. Bei, E.P. George, Relative effects of enthalpy and entropy on the phase stability of equiatomic high-entropy alloys, Acta Mater 61 (2013) 2628–2638.

[15] L. Zhang, Y. Xiang, J. Han, D.J. Srolovitz, The effect of randomness on the strength of high-entropy alloys, Acta Mater 166 (2019) 424–434.

[16] Q. Ding, Y. Zhang, X. Chen, X. Fu, D. Chen, S. Chen, L. Gu, F. Wei, H. Bei, Y. Gao, M. Wen, J. Li, Z. Zhang, T. Zhu, R.O. Ritchie, Q. Yu, Tuning element distribution, structure and properties by composition in high-entropy alloys, Nature 574 (2019) 223–227.

[17] R. Zhang, S. Zhao, J. Ding, Y. Chong, T. Jia, C. Ophus, M. Asta, R.O. Ritchie, A.M. Minor, Short-range order and its impact on the CrCoNi medium-entropy alloy, Nature 581 (2020) 283–287.

[18] A. Tamm, A. Aabloo, M. Klintenberg, M. Stocks, A. Caro, Atomic-scale properties of Ni-based FCC ternary, and quaternary alloys, Acta Mater 99 (2015) 307–312.

[19] E. Antillon, C. Woodward, S.I. Rao, B. Akdim, T.A. Parthasarathy, Chemical short range order strengthening in a model FCC high entropy alloy, Acta Mater 190 (2020) 29–42.

[20] W.-R. Jian, Z. Xie, S. Xu, Y. Su, X. Yao, I.J. Beyerlein, Effects of lattice distortion and chemical short-range order on the mechanisms of deformation in medium entropy alloy CoCrNi, Acta Mater 199 (2020) 352–369.

[21] Q.-J. Li, H. Sheng, E. Ma, Strengthening in multi-principal element alloys with local-chemical-order roughened dislocation pathways, Nature Commun 10 (2019) 3563.

[22] B. Yin, S. Yoshida, N. Tsuji, W.A. Curtin, Yield strength and misfit volumes of NiCoCr and implications for short-range-order, Nature Commun 11 (2020) 2507.
[23] Y. Wu, F. Zhang, X. Yuan, H. Huang, X. Wen, Y. Wang, M. Zhang, H. Wu, X. Liu, H. Wang, S. Jiang, Z. Lu, Short-range ordering and its effects on mechanical properties of high-entropy alloys, J. Mater. Sci. Technol. 62 (2021) 214–220.
[24] Y.-J. Liang, L. Wang, Y. Wen, B. Cheng, Q. Wu, T. Cao, Q. Xiao, Y. Xue, G. Sha, Y. Wang, Y. Ren, X. Li, L. Wang, F. Wang, H. Cai, High-content ductile coherent nanoprecipitates achieve ultrastrong high-entropy alloys, Nature Commun 9 (2018) 4063.
[25] F.-H. Cao, Y.-J. Wang, L.-H. Dai, Novel atomic-scale mechanism of incipient plasticity in a chemically complex CrCoNi medium-entropy alloy associated with inhomogeneity in local chemical environment, Acta Mater 194 (2020) 283–294.
[26] A. Sharma, S.A. Deshmukh, P.K. Liaw, G. Balasubramanian, Crystallization kinetics in AlxCrCoFeNi ($0\leq x\leq 40$) high-entropy alloys, Scr. Mater. 141 (2017) 54–57.
[27] J. Li, Q. Fang, B. Liu, Y. Liu, Transformation induced softening and plasticity in high entropy alloys, Acta Mater 147 (2018) 35–41.
[28] C. Niu, W. Windl, M. Ghazisaeidi, Multi-cell Monte Carlo relaxation method for predicting phase stability of alloys, Scr. Mater. 132 (2017) 9–12.
[29] W.-M. Choi, Y.H. Jo, S.S. Sohn, S. Lee, B.-J. Lee, Understanding the physical metallurgy of the CoCrFeMnNi high-entropy alloy: an atomistic simulation study, npj Comput. Mater. 4 (2018) 1.
[30] Y. Lederer, C. Toher, K.S. Vecchio, S. Curtarolo, The search for high entropy alloys: a high-throughput ab-initio approach, Acta Mater 159 (2018) 364–383.
[31] T. Kostiuchenko, F. Körmann, J. Neugebauer, A. Shapeev, Impact of lattice relaxations on phase transitions in a high-entropy alloy studied by machine-learning potentials, npj Comput. Mater. 5 (2019) 1–7.
[32] H. Zhang, X. Sun, S. Lu, Z. Dong, X. Ding, Y. Wang, L. Vitos, Elastic properties of AlxCrMnFeCoNi ($0 \leq x \leq 5$) high-entropy alloys from ab initio theory, Acta Mater 155 (2018) 12–22.
[33] D. Wei, X. Li, J. Jiang, W. Heng, Y. Koizumi, W.-M. Choi, B.-J. Lee, H.S. Kim, H. Kato, A. Chiba, Novel Co-rich high performance twinning-induced plasticity (TWIP) and transformation-induced plasticity (TRIP) high-entropy alloys, Scr. Mater. 165 (2019) 39–43.
[34] Z. Fu, W. Chen, H. Wen, D. Zhang, Z. Chen, B. Zheng, Y. Zhou, E.J. Lavernia, Microstructure and strengthening mechanisms in an FCC structured single-phase nanocrystalline Co25Ni25Fe25Al7.5Cu17.5 high-entropy alloy, Acta Mater 107 (2016) 59–71.
[35] Y.H. Jo, S. Jung, W.M. Choi, S.S. Sohn, H.S. Kim, B.J. Lee, N.J. Kim, S. Lee, Cryogenic strength improvement by utilizing room-temperature deformation twinning in a partially recrystallized VCrMnFeCoNi high-entropy alloy, Nature Commun 8 (2017) 15719.
[36] F. Otto, A. Dlouhý, Ch. Somsen, H. Bei, G. Eggeler, E.P. George, The influences of temperature and microstructure on the tensile properties of a CoCrFeMnNi high-entropy alloy, Acta Mater 61 (2013) 5743–5755.
[37] X.D. Xu, P. Liu, S. Guo, A. Hirata, T. Fujita, T.G. Nieh, C.T. Liu, M.W. Chen, Nanoscale phase separation in a fcc-based CoCrCuFeNiAl0.5 high-entropy alloy, Acta Mater 84 (2015) 145–152.
[38] Z. Wang, I. Baker, Z. Cai, S. Chen, J.D. Poplawsky, W. Guo, The effect of interstitial carbon on the mechanical properties and dislocation substructure evolution in Fe40.4Ni11.3Mn34.8Al7.5Cr6 high entropy alloys, Acta Mater 120 (2016) 228–239.
[39] D. Choudhuri, B. Gwalani, S. Gorsse, M. Komarasamy, S.A. Mantri, S.G. Srinivasan, R.S. Mishra, R. Banerjee, Enhancing strength and strain hardenability via deformation twinning in fcc-based high entropy alloys reinforced with intermetallic compounds, Acta Mater 165 (2019) 420–430.
[40] A. Sharma, P. Singh, D.D. Johnson, P.K. Liaw, G. Balasubramanian, Atomistic clustering-ordering and high-strain deformation of an Al0.1CrCoFeNi high-entropy alloy, Sci. Rep. 6 (2016) 31028.
[41] L.J. Santodonato, Y. Zhang, M. Feygenson, C.M. Parish, M.C. Gao, R.J.K. Weber, J.C. Neuefeind, Z. Tang, P.K. Liaw, Deviation from high-entropy configurations in the atomic distributions of a multi-principal-element alloy, Nature Commun 6 (2015) 5964.
[42] S. Plimpton, Fast parallel algorithms for short-range molecular dynamics, J. Comput. Phys. 117 (1995) 1–19.
[43] X.W. Zhou, H.N.G. Wadley, R.A. Johnson, D.J. Larson, N. Tabat, A. Cerezo, A.K. Petford-Long, G.D.W. Smith, P.H. Clifton, R.L. Martens T. F. Kelly, Atomic scale structure of sputtered metal multilayers, Acta Mater 49 (2001) 4005–4015.
[44] X.W. Zhou, R.A. Johnson, H.N.G. Wadley, Misfit-energy-increasing dislocations in vapor-deposited CoFe/NiFe multilayers, Phys. Rev. B 69 (2004) 144113.
[45] W. Li, H. Fan, J. Tang, Q. Wang, X. Zhang, J.A. El-Awady, Effects of alloying on deformation twinning in high entropy alloys, Mater. Sci. Eng. A 763 (2019) 138143.
[46] S. Chen, Z.H. Aitken, Z. Wu, Z. Yu, R. Banerjee, Y.-W. Zhang, Hall-Petch and inverse Hall-Petch relations in high-entropy CoNiFeAlxCu1-x alloys, Mater. Sci. Eng. A 773 (2020) 138873.
[47] W.-R. Wang, W.-L. Wang, S.-C. Wang, Y.-C. Tsai, C.-H. Lai, J.-W. Yeh, Effects of Al addition on the microstructure and mechanical property of AlxCoCrFeNi high--entropy alloys, Intermetallics 26 (2012) 44–51.
[48] N. Metropolis, A.W. Rosenbluth, M.N. Rosenbluth, A.H. Teller, E. Teller, Equation of state calculations by fast computing machines, J. Chem. Phys. 21 (1953) 1087–1092.
[49] A. Stukowski, Visualization and analysis of atomistic simulation data with OVITO-the open visualization tool, Model. Simulat. Mater. Sci. Eng. 18 (2009) 15012.
[50] A. Zunger, S.-H. Wei, L.G. Ferreira, J.E. Bernard, Special quasirandom structures, Phys. Rev. Lett. 65 (1990) 353–356.
[51] C. Jiang, B.P. Uberuaga, Efficient ab initio modeling of random multicomponent alloys, Phys. Rev. Lett. 116 (2016) 105501.
[52] M.C. Gao, J.W. Yeh, P.K. Liaw, Y. Zhang, in: High-Entropy alloys: fundamentals and applications, Springer International Publishing, Cham, Switzerland, 2016, pp. 399–444.
[53] J.M. Cowley, X-ray measurement of order in single crystals of Cu3Au, J. Appl. Phys. 21 (1950) 24–30.
[54] C. Tang, C.H. Wong, Formation of chemical short range order and its influences on the dynamic/mechanical heterogeneity in amorphous Zr–Cu–Ag alloys: A molecular dynamics study, Intermetallics 70 (2016) 61–67.
[55] G. Kresse, J. Furthmüller, Efficient iterative schemes for ab initio total-energy calculations using a plane-wave basis set, Phys. Rev. B 54 (1996) 11169–11186.
[56] P.E. Blöchl, Projector augmented-wave method, Phys. Rev. B 50 (1994) 17953–17979.
[57] G. Kresse, D. Joubert, From ultrasoft pseudopotentials to the projector augmented-wave method, Phys. Rev. B 59 (1999) 1758–1775.
[58] J.P. Perdew, K. Burke, M. Ernzerhof, Generalized gradient approximation made simple, Phys. Rev. Lett. 77 (1996) 3865–3868.
[59] J.B. Mann, T.L. Meek, L.C. Allen, Configuration energies of the d-block elements, J. Am. Chem. Soc. 122 (2000) 5132–5137.
[60] B. Yin, W.A. Curtin, Origin of high strength in the CoCrFeNiPd high-entropy alloy, Mater. Res. Lett. 8 (2020) 209–215.